

Polarization-sensitive reconstruction of transient local THz fields at dielectric interfaces: supplementary material

KAY WALTAR¹, JOHANNES HAASE², RUI PAN³, TORSTEN GOLZ³, PAVEL KLIUIEV¹, MICHAEL WEINL⁴, MATTHIAS SCHRECK⁴, SAŠA BAJT³, NIKOLA STOJANOVIC³, JEROEN A. VAN BOKHOVEN⁵, MATTHIAS HENGESBERGER¹, JUERG OSTERWALDER¹, AND LUCA CASTIGLIONI^{1,*}

¹Physics Department, University of Zurich, Zurich, Switzerland

²Laboratory for Catalysis and Sustainable Chemistry, Paul Scherrer Institute, Villigen, Switzerland

³Deutsches Elektronen-Synchrotron-DESY, Hamburg, Germany

⁴Institut für Physik, Universität Augsburg, D-86135 Augsburg, Germany

⁵Institute for Chemical and Bioengineering, ETH Zurich, Zurich, Switzerland

*Corresponding author: castiglioni@physik.uzh.ch

Published 13 November 2019

This document provides supplementary information to "Polarization-sensitive reconstruction of transient local THz fields at dielectric interfaces," <https://doi.org/10.1364/OPTICA.6.001431>.

1. DETAILS OF THE THZ/X-RAY PUMP PROBE EXPERIMENT

The THz/x-ray pump-probe experiments were performed at the THz beamline of the free electron laser FLASH at DESY. Figure 2(a) in the main text schematically displays the experimental setup. THz radiation is generated by an undulator in series with the main x-ray undulator [1, 2]. THz and x-ray pulses are synchronized down to a temporal jitter of 5 fs since they are generated by the same electron bunch [3]. The effective repetition rate was 2.5 kHz (250 bunches/bunch-train, rep. rate 10 Hz). In the present experiment the central THz undulator frequency was set to 2 THz ($\lambda = 150 \mu\text{m}$) and the fundamental wavelength of the x-ray pulses was 24.6 nm. The 3rd harmonic was filtered out to be the dominant x-ray contribution by means of a noble gas attenuator, metallic absorber foils [1, 4] and a multi-layer mirror. The corresponding x-ray photon energy is 151.2 eV.

Before entering the ultra-high vacuum (UHV) endstation, the x-ray light is back-reflected and focussed at a near-normal incidence spherical multilayer mirror ($f = 3.5 \text{ m}$). The super polished glass substrate with a diameter of 25.4 mm was coated in DESY's multilayer laboratory with a custom developed Ru/B₄C multilayer (110 bilayers) and characterized at the PTB beamline (Bessy II, Berlin). It showed a peak reflectivity of 18% at

8.12 nm (3° off-normal) with a bandwidth of 0.08 nm (FWHM). The above mentioned geometry is necessary to account for the inherent optical path difference between THz and x-ray beams [5]. The THz beam is redirected through the THz beamline hutch with the possibility of EO sampling and further through a delay stage with optional band-pass filtering.

Figure 2(b) in the main text shows the experimental geometry inside the UHV endstation [6]. The incoming THz light is tightly focused onto the sample by means of a gold-coated, 30° off-axis parabolic mirror ($f = 27.2 \text{ mm}$). The angle of incidence onto the sample is 60°. The x-ray light enters the interaction region from the backside of the parabolic mirror through a small hole. The spot-size estimated for the x-ray pulse at the sample position is about 200 μm (FWHM) and the spot-size of the THz is about 500 μm (FWHM). The duration of individual light pulses is estimated to be shorter than 100 fs for the x-ray and about 5 ps for the THz light. The polarization of the clean undulator radiation is oriented parallel (p-polarized) to the plane of light incidence (yz -plane in Fig. 2(a) of main text) in case of x-ray and perpendicular (s-polarized) for the THz light. The emitted electrons are collected in a hemispherical analyzer with a wide acceptance angle. The angle-dispersive axis of the analyzer was parallel to the polarization of the THz pulse (x -axis).

2. ELECTRIC FIELD RECONSTRUCTION

The polarization-sensitive reconstruction of all field components based on angle-resolved photoemission data was previously developed in our group and verified by Monte-Carlo simulations. We thus only briefly discuss the essential steps here and relegate to our earlier work [7] for the details. Under the influence of an external electric field, *i.e.* the time-varying field of the pump pulse, the individual electron momentum changes according to the canonical momentum relation

$$\vec{p} = \vec{p}_0 + q\vec{A}(\tau). \quad (\text{S1})$$

In addition to their initial momentum \vec{p}_0 due to the photoemission process, the electrons undergo a momentum modification $\Delta\vec{p} = q\vec{A}(\tau)$ in the external electric field. Here, q is the charge of the electron and $\vec{A}(\tau)$ the vectorpotential of the external field at the time of photoemission τ . Since $\vec{A}(\infty)$, *i.e.* the vectorpotential at the time of detection, vanishes, $\vec{A}(\tau)$ can be directly related to the electric field by a simple derivative with respect to the photoemission time:

$$\vec{E}(t) = \partial_\tau \vec{A}(\tau) |_{\tau=t}. \quad (\text{S2})$$

Since the electrons start with finite initial momenta the total momentum change $\Delta\vec{p}$ is acquired at different locations on a path along which the electrons move in the complex distribution of the external electric field. An electric field reconstructed in this scheme is an effective field that is averaged along the electron path.

Electric field components linearly polarized parallel (E_{\parallel}) or perpendicular (E_{\perp}) to the sample surface lead to distinct modifications of the photoelectron momentum distribution. Figure S1(a) schematically displays these modifications of the initial distribution \vec{p}_0 by a pure parallel field component. The momentum gained in the external field $\Delta\vec{p}$ leads to an antisymmetrical shift of the momentum distribution with respect to the normal emission direction. In Fig. S1(b) the same situation is presented for the case of a pure perpendicular field component. The final distribution \vec{p}' is the result of a symmetrical shift along the surface normal. Schematic analyzer images are presented in Fig. 1(c) (main text) in order to illustrate the reconstruction scheme of the electric field components. At every time delay between pump and probe pulse the acquired analyzer image is analyzed with regard to momentary modifications of the electron momentum distribution. The energetic center of mass (COM), *e.g.* the center position of an elastic photoemission line, is experimentally determined in each angular channel of the analyzer. The relative COM shift as compared to an undisturbed distribution, *i.e.* the momentum distribution at large negative delays ($t \ll t_0$), is a measure of the streaking field strength. The tilt angle of the COM distribution with respect to the angle-dispersive axis of the analyzer serves as measure of the parallel field component whereas the kinetic energy offset in the normal emission channel is a measure of the perpendicular field component. With an algebraic addition of initial and gained momenta an analytical relation between the observed kinetic energy offset along normal emission and the perpendicular field component can be established:

$$|\Delta\vec{p}| = |\vec{p}_0| \cdot \left(\sqrt{1 + \frac{2m_e\Delta E}{|\vec{p}_0|^2}} - 1 \right) = \sqrt{2m_eE} \left(\sqrt{1 + \frac{\Delta E}{E}} - 1 \right). \quad (\text{S3})$$

Here, E is the initial kinetic energy, ΔE the kinetic energy offset at normal emission and m_e is the free electron mass. In case of the parallel field component the unknown initial emission direction precludes an analytical solution. However, the tilt direction of the COM distribution is a hallmark of the parallel field direction and the amplitude can be obtained by a fitting procedure. The temporal shape of the experimentally determined tilt angle is used as the initial vector potential input of the parallel field component. A fitting parameter is used to obtain the best match between the experimentally observed and the model-predicted tilt angle at each time delay.

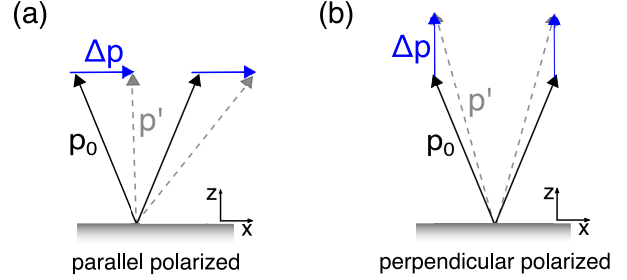


Fig. S1. Field-induced modification of electron momentum. (a) Illustration of the effect of a purely parallel electric field (E_{\parallel}) on the initial photoelectron momentum distribution. The initial electron momentum \vec{p}_0 is modified by $\Delta\vec{p}$ due to interaction with the electric field. The final momentum is \vec{p}' . (b) The effect of a perpendicular electric field (E_{\perp}) on the initial photoelectron momentum distribution.

3. SAMPLE PREPARATION AND CHARACTERIZATION

The investigated thin film samples consist of a 10 nm (nominal thickness) layer of Pt grown along the (111) direction in an island-like fashion. The films were grown on top of a 0.5 mm Si(111) wafer with a 40 nm YSZ interlayer [8]. Figure 2(c) in the main text presents a sketch of the layered thin film structure. SEM images of the sample suggest individual Pt islands with sizes smaller than 300 nm. X-ray photoelectron diffraction (bottom, left) and low energy electron diffraction (LEED) data (bottom, right) confirm the (111) orientation of the Pt islands with low mosaicity and twinning. Both the thin film samples and the Pt(111) bulk single crystal were subject to standard cycles of Ar^+ sputtering and annealing prior to the experiments. Cleanliness and surface quality were verified by x-ray photoelectron spectroscopy and LEED.

4. ALIGNMENT OF THE OFF-AXIS PARABOLIC MIRROR

A slight misalignment of the off-axis parabolic mirror leads to a modified polarization of the incoming THz light at the sample surface. Figure S2 shows the effect of a slight tilt of the parabolic mirror about two axes: the direction of detection (z) and the direction of propagation of the THz light entering the endstation (y). The effective polarization in the xz -plane is presented by the position in the polar plot. Each individual color in Fig. S2 represents a certain value of γ , *i.e.* the tilt angle around the z -axis that has been varied in steps of 0.5° . For each γ the value of δ , *i.e.* the tilt angle about the y -axis, has been varied between 0 and 5° in steps of 0.5° . While a tilt δ around the y -axis does not lead to major changes in the overall polarization direction, the effect of a tilt γ leads to profound changes in

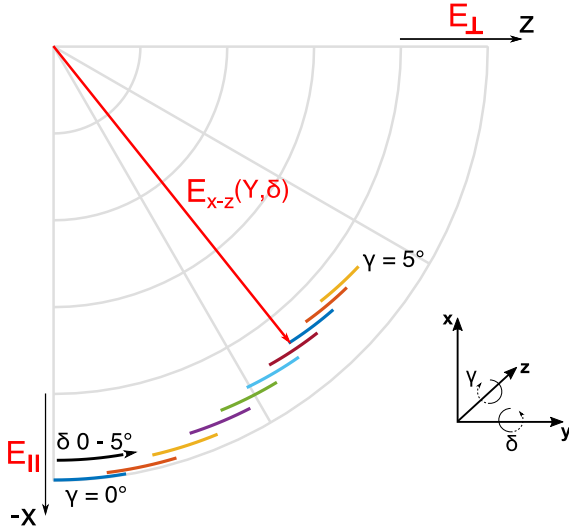


Fig. S2. Effect of slight Misalignment of parabolic mirror about two axes y and z . The definition of the axes refers to those used in the main article. The calculated polarization in the xz -plane as a function of two distinct tilts of the parabolic mirror is represented in a polar plot.

the polarization direction even for small changes of $0.5 - 1^\circ$. The decreasing radius with larger γ indicates an increase of polarization components perpendicular to the xz -plane.

5. BACK-REFLECTION AT THE SAMPLE HOLDER

The incoming light is reflected at different interfaces in the multilayered thin-film structure that is schematically depicted in Figure S3(a). The THz grating is a result of the superposition of the incoming THz field with an amplitude E_{\parallel}^0 (Fig. S3(a), black) and the light that is directly reflected at the vacuum/YSZ and YSZ/Si interfaces. The amplitude of this directly reflected field is E_{\parallel}^R (Fig. S3(a), green). Due to the large THz wavelength compared to the dimensions of the YSZ-layer there is no geometrical phase shift between the two reflections. The part of the incoming light that is transmitted into the Si-slab is back-reflected at the Mo sample holder and leaves the sample surface with a time delay of 11.7 ps and an amplitude E_{\parallel}^T (Fig. S3(a), red). Using the experimental value of the amplitude of the back-reflected pulse, the incoming and directly reflected THz amplitudes can be calculated by

$$E_{\parallel}^T = t_{\parallel}^{\text{vac,YSZ}} \cdot t_{\parallel}^{\text{YSZ,Si}} \cdot t_{\parallel}^{\text{Si,YSZ}} \cdot t_{\parallel}^{\text{YSZ,vac}} \cdot E_{\parallel}^0 \quad (\text{S4})$$

$$E_{\parallel}^R = (r_{\parallel}^{\text{YSZ,vac}} + t_{\parallel}^{\text{vac,YSZ}} \cdot r_{\parallel}^{\text{Si,YSZ}} \cdot t_{\parallel}^{\text{YSZ,vac}}) \cdot E_{\parallel}^0. \quad (\text{S5})$$

Here, the superscript indices of the Fresnel reflection ($r_{\parallel}^{j,i}$) and transmission ($t_{\parallel}^{j,i}$) coefficients refer to the interface and direction of the incoming wave, i.e. $t_{\parallel}^{\text{YSZ,vac}}$ describes the transmission coefficient of a wave entering a vacuum/YSZ interface from the vacuum. The Fresnel coefficients depend on the refractive index of the materials at the respective THz frequency [9]. For the YSZ layer this value is not precisely known and depends on the method by which this layer was grown [10–12]. Taking the experimental value of $6 \cdot 10^6 \text{ Vm}^{-1}$ for E_{\parallel}^T , i. e. the amplitude of the back-reflected (2^{nd}) pulse on the thin-film sample, the

amplitude values obtained in Figure S3(b) are in good agreement with the experimentally determined values of the parallel field component in the first pulse reconstructed on the thin-film sample. Hence the assumed model of the thin-film structure is consistent with the experimental data.

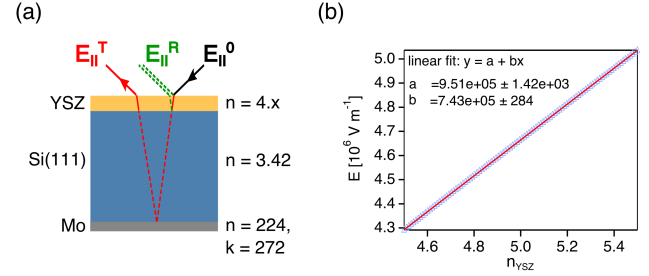


Fig. S3. Sketch of THz back-reflection at the multilayer thin-film structure. The amplitudes of the incoming and reflected THz fields are depicted in different colors. The refractive indices of the YSZ- and Si- layers are also shown.

6. ELECTRIC FIELD SIMULATIONS

Simulations of the electric field distribution in Figure 4 in the main text were performed with the wave optics module of the COMSOL Multiphysics software. The thin film sample is modeled as a dielectric layer of YSZ on a slab of Si. The thin Pt film is modeled by a single island, 200 nm in width and 10 nm in height. Optical parameters for the platinum island at 2 THz are taken from the extrapolation of the Brendel-Bormann model [13] for bulk metals. Metal clusters of more than 10 nm size are expected to show bulk conductivity [14]. The total field in close proximity to the island is presented at a specific phase of the external driving field. The initial power flow was identical in all simulations.

REFERENCES

1. K. Tiedtke, A. Azima, N. von Bargen, L. Bittner, S. Bonfigt, S. Düsterer, B. Faatz, U. Frühling, M. Gensch, C. Gerth, N. Guerassimova, U. Hahn, T. Hans, M. Hesse, K. Honkavaar, U. Jastrow, P. Juranic, S. Kapitzki, B. Keitel, T. Kracht, M. Kuhlmann, W. B. Li, M. Martins, T. Núñez, E. Plönjes, H. Redlin, E. L. Saldin, E. A. Schneidmiller, J. R. Schneider, S. Schreiber, N. Stojanovic, F. Tavella, S. Toleikis, R. Treusch, H. Weigelt, M. Wellhöfer, H. Wabnitz, M. V. Yurkov, and J. Feldhaus, “The soft x-ray free-electron laser flash at desy: beamlines, diagnostics and end-stations,” *New J. Phys.* **11**, 023029 (2009).
2. B. Green, S. Kovalev, V. Asegar, G. Geloni, U. Lehnert, T. Golz, M. Kuntzsch, C. Bauer, J. Hauser, J. Voigtlaender, B. Wustmann, I. Koesterke, M. Schwarz, M. Freitag, A. Arnold, J. Teichert, M. Justus, W. Seidel, C. Ilgner, N. Awari, D. Nicoletti, S. Kaiser, Y. Laplace, S. Rajasekaran, L. Zhang, S. Winnerl, H. Schneider, G. Schay, I. Lorincz, A. A. Rauscher, I. Radu, S. Mährlein, T. H. Kim, J. S. Lee, T. Kampfrath, S. Wall, J. Heberle, A. Malnasi-Csizmadia, A. Steiger, A. S. Müller, M. Helm, U. Schramm, T. Cowan, P. Michel, A. Cavalleri, A. S. Fisher, N. Stojanovic, and M. Gensch, “High-field High-Repetition-Rate Sources for the Coherent THz Control of Matter,” *Sci. Rep.* **6**, 22256 EP – (2016).

3. F. Tavella, N. Stojanovic, G. Geloni, and M. Gensch, "Few-femtosecond timing at fourth-generation X-ray light sources," *Nat. Photon.* **5**, 162–165 (2011).
4. M. Richter, A. Gottwald, U. Kroth, A. A. Sorokin, S. V. Bobashev, L. A. Shmaenok, J. Feldhaus, C. Gerth, B. Steeg, K. Tiedtke, and R. Treusch, "Measurement of gigawatt radiation pulses from a vacuum and extreme ultraviolet free-electron laser," *Appl. Phys. Lett.* **83**, 2970–2972 (2003).
5. E. Zapolnova, T. Golz, R. Pan, K. Klose, S. Schreiber, and N. Stojanovic, "THz pulse doubler at FLASH: Double pulses for pump-probe experiments at X-ray FELs," *J. Synchrotron Rad.* **25**, 39–43 (2018).
6. M. Greif, L. Castiglioni, D. Becker-Koch, J. Osterwalder, and M. Hengsberger, "Acquisition of photoelectron diffraction patterns with a two-dimensional wide-angle electron analyzer," *J. Electron. Spectrosc. Relat. Phenom.* **197**, 30–36 (2014).
7. K. Waltar, J. Haase, M. Lucchini, J. A. van Bokhoven, M. Hengsberger, J. Osterwalder, and L. Castiglioni, "Polarization-sensitive pulse reconstruction by momentum-resolved photoelectron streaking," *Opt. Express* **26**, 8364–8374 (2018).
8. M. Fischer, R. Brescia, S. Gsell, M. Schreck, T. Brugger, T. Greber, J. Osterwalder, and B. Stritzker, "Growth of twin-free heteroepitaxial diamond on Ir/YSZ/Si(111)," *J. Appl. Phys.* **104**, 123531 (2008).
9. J. Dai, J. Zhang, W. Zhang, and D. Grischkowsky, "Terahertz time-domain spectroscopy characterization of the far-infrared absorption and index of refraction of high-resistivity, float-zone silicon," *J. Opt. Soc. Am. B* **21**, 1379–1386 (2004).
10. D. Grischkowsky and S. Keiding, "THz time-domain spectroscopy of high Tc substrates," *Appl. Phys. Lett.* **57**, 1055–1057 (1990).
11. C. Maiti, G. Dalapati, S. Chatterjee, S. Samanta, S. Varma, and S. Patil, "Electrical properties of high permittivity ZrO₂ gate dielectrics on strained-Si," *Solid-State Electron.* **48**, 2235–2241 (2004).
12. T. Fukuchi, N. Fuse, M. Okada, T. Fujii, M. Mizuno, and K. Fukunaga, "Measurement of Refractive Index and Thickness of Topcoat of Thermal Barrier Coating by Reflection Measurement of Terahertz Waves," *Electron. Commun. Jpn.* **132-A**, 702–708 (2012).
13. A. D. Rakić, A. B. Djurišić, J. M. Elazar, and M. L. Majewski, "Optical properties of metallic films for vertical-cavity optoelectronic devices," *Appl. Opt.* **37**, 5271–5283 (1998).
14. V. V. Datsyuk and I. V. Ivanytska, "Statistical and electrical properties of the conduction electrons of a metal nanosphere in the region of metal-insulator transition," *Nanoscale Res. Lett.* **9**, 174 (2014).